



CrossMark  
click for updates

Cite this: *RSC Adv.*, 2016, 6, 51777

# The formation and mechanism of nano-monocrystalline $\gamma$ -Fe<sub>2</sub>O<sub>3</sub> with graphene-shell for high-performance lithium ion batteries†

Jiangtao Hu,‡ Wen Li,‡ Chaokun Liu, Hanting Tang, Tongchao Liu, Hua Guo, Xiaohu Song, Jiabin Zheng, Yidong Liu, Yandong Duan\* and Feng Pan\*

Using a sintering process with Prussian Blue (PB) and 20 wt% glucose at high temperature (950 °C for 6 hours in Ar/H<sub>2</sub>) with oxidation in the air at room temperature, we synthesized a nano-monocrystalline  $\gamma$ -phase iron oxide ( $\gamma$ -Fe<sub>2</sub>O<sub>3</sub>) compound coated with carbon comprising a number of graphene layers, which was named as core-shell nano-monocrystalline  $\gamma$ -Fe<sub>2</sub>O<sub>3</sub>@graphene. It can be noted that the formation of nano-monocrystal is different from forming core-shell nano-polycrystalline hollow  $\gamma$ -Fe<sub>2</sub>O<sub>3</sub>@graphene sintered at lower temperature (650 °C 6 hours in Ar) via a simple Kirkendall process with oxidation at room temperature as reported in our previous study. We further investigate how nano-monocrystalline  $\gamma$ -Fe<sub>2</sub>O<sub>3</sub> is formed by controlling the synthesis process and testing with TEM and SEM. We confirmed that the nano-monocrystalline  $\gamma$ -Fe<sub>2</sub>O<sub>3</sub> is grown from nano-monocrystalline Fe with interface catalysis of O<sub>2</sub> and the related mechanism is discussed through comparing the structures of  $\gamma$ -Fe<sub>2</sub>O<sub>3</sub> and the Fe crystals. The core-shell nano-monocrystalline  $\gamma$ -Fe<sub>2</sub>O<sub>3</sub>@graphene shows high performance as an anode material in Li-ions batteries (much better than nano-polycrystalline hollow  $\gamma$ -Fe<sub>2</sub>O<sub>3</sub>@graphene reported in previous study). For example, the cycling stability and rate performance are remarkable as an anode material for lithium ion batteries with a high reversible capacity of 848.08 and 782.54 mA h g<sup>-1</sup> at 1C and 5C for 600 cycles, respectively, and a high rate performance (284.42 mA h g<sup>-1</sup> at 20C). Another interesting performance is that during the first 80 cycles, the specific capacity increases, which may result from more interface area being generated by the  $\gamma$ -Fe<sub>2</sub>O<sub>3</sub> nano-monocrystal crushing with protection of the graphene-shell during the initial charging/discharging cycles. This synthesis method and mechanism can be used as a guide to produce  $\gamma$ -Fe<sub>2</sub>O<sub>3</sub> as an anode material for lithium ion batteries with high performance on a large scale.

Received 30th March 2016  
Accepted 13th May 2016

DOI: 10.1039/c6ra08143f

www.rsc.org/advances

## Introduction

To solve the current energy and environmental problems, many significant studies have been devoted for developing advanced lithium-ion batteries (LIB) in recent decades, which are widely used in portable electronics and electric vehicles (EVs).<sup>1–3</sup> Graphite and other carbon materials are the common commercial anode materials with a theoretical capacity of 372 mA h g<sup>-1</sup>. Unfortunately, this capacity cannot meet the energy demands of current devices. Therefore, searching for a low cost anode material with high capacity and security is imperative. For this purpose, transition metal oxides have attracted increased interest. In particular, Fe<sub>2</sub>O<sub>3</sub> has been paid more

attention than Fe<sub>3</sub>O<sub>4</sub>, SnO<sub>2</sub>, and Bi<sub>2</sub>O<sub>3</sub> (ref. 4–9) due to its high theoretical capacity (1007 mA h g<sup>-1</sup>), abundance, low cost, and environmentally benign nature.<sup>10,11</sup> However, like other transition metal oxides, Fe<sub>2</sub>O<sub>3</sub> undergoes volume changes during the discharge and charge processes, which results in the capacity fading. In addition, the electrical conductivity of these electrode materials is also very low, which limits their specific capacities and rate capabilities.<sup>12–14</sup>

Considerable research has been carried out to solve the abovementioned problems, such as reducing the particle size,<sup>6,15</sup> preparing hybrids with graphene/nanotube/other carbon materials,<sup>16–18</sup> and developing different structures (hollow/core-shell).<sup>19,20</sup> In particular, graphene, which provides high conductivity, light weight, high mechanical strength, structural flexibility, and large surface area, has been widely used in hybrid nanocomposites for electrode materials.<sup>21–23</sup> Benefitting from these methods, the electrochemical performance of Fe<sub>2</sub>O<sub>3</sub> has been greatly improved as an anode material. However, the synthetic process used to prepare graphene is complex and its cost is relatively expensive. In our previous

School of Advanced Materials, Peking University Shenzhen Graduate School, Peking University, Shenzhen 518055, China. E-mail: panfeng@pkusz.edu.cn; Tel: +86-755-26033200

† Electronic supplementary information (ESI) available: Figures of the crystal structure, TEM and impedance. See DOI: 10.1039/c6ra08143f

‡ J. Hu and W. Li contributed equally to this work.

study, we synthesized a core-shell structure with graphene as the shell and nano-polycrystalline hollow  $\gamma$ -Fe<sub>2</sub>O<sub>3</sub> as the core (core-shell nano-hollow- $\gamma$ -Fe<sub>2</sub>O<sub>3</sub>@graphene) sintered at low temperature (650 °C for 6 h in Ar) *via* a simple Kirkendall process at room temperature.<sup>20</sup> In this study, to be different from the core-shell nano-hollow  $\gamma$ -Fe<sub>2</sub>O<sub>3</sub>@graphene composite, we have synthesized a nano-monocrystalline  $\gamma$ -Fe<sub>2</sub>O<sub>3</sub>@graphene composite by sintering Prussian Blue (PB) and 20 wt% glucose at high temperature (950 °C for 6 h in Ar/H<sub>2</sub>) *vs.* the low temperature (650 °C) used to form poly-crystalline  $\gamma$ -Fe<sub>2</sub>O<sub>3</sub>@graphene in the previously reported study. To find the mechanism of formation of the nano-monocrystals, we designed experiments and found that nano-monocrystalline Fe is formed and then transformed into monocrystalline  $\gamma$ -Fe<sub>2</sub>O<sub>3</sub> when placed into air at room temperature. The mechanism is discussed by comparing the structures of  $\gamma$ -Fe<sub>2</sub>O<sub>3</sub> and the Fe crystals. Interestingly, the core-shell nano-monocrystalline  $\gamma$ -Fe<sub>2</sub>O<sub>3</sub>@graphene shows much higher electrochemical performance as an anode material for Li-ions batteries than nano-polycrystalline hollow  $\gamma$ -Fe<sub>2</sub>O<sub>3</sub>@graphene used in the previous report, including much better cycle stability, remarkable rate capability, and high capacity.

## Experimental

### Materials

The graphene coated monocrystalline  $\gamma$ -Fe<sub>2</sub>O<sub>3</sub> was synthesized *via* a facile annealing method. A certain amount of Prussian Blue (PB) (1.0 g) and 20 wt% glucose (0.2 g) were dispersed in a mixed solution containing water and alcohol. Then, the abovementioned slurry was ground in a mortar to ensure homogenous mixing of the PB and glucose. After the abovementioned steps, we placed the sticky compound into an air-dry oven (80 °C for 4 h) and then transferred the mixture to a tube furnace under the condition of 950 °C for 6 hours in Ar/H<sub>2</sub> (v/v = 95/5). After the tube furnace was cooled down to room temperature, the mixture was taken out and vibrated heavily to make sure that the generated particles were oxidized completely. During this step, we have observed a phenomenon of spontaneous combustion for a long time. After the abovementioned steps, the graphene coated  $\gamma$ -Fe<sub>2</sub>O<sub>3</sub> material was thereby synthesized.

### Material characterization

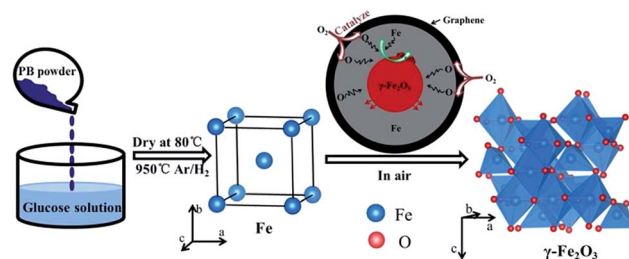
X-ray powder diffraction (XRD, Bruker D8 Advance diffractometer) measurements were performed to obtain structural information on the composites using Cu-K $\alpha$  radiation ( $\lambda = 1.54 \text{ \AA}$ ). The morphology and size distribution were recorded using scanning electron microscopy (SEM, ZEISS Supra 55) and transmission electron microscopy (TEM, FEITecnaïG2 30), respectively. X-ray photoelectron spectroscopy (XPS) measurements were taken using an ESCALAB 250XL. Raman measurements were carried out on a HORIBA Jobin Yvon spectrometer. To identify the carbon content, thermogravimetric analysis (TGA) was performed in air atmosphere on a TGA/DSC1 system at a heating rate of 10 °C min<sup>-1</sup> between 30 °C and 900 °C.

### Electrochemical measurements

The prepared  $\gamma$ -Fe<sub>2</sub>O<sub>3</sub>@graphene was blended with Super P carbon black and a binder (polyvinylidenedifluoride, PVDF) at a weight ratio of 60 : 30 : 10 in *N*-methylpyrrolidone (NMP) to form slurry. After continuous stirring, the homogeneous slurry was spread on a copper foil. The copper foil was then dried at 80 °C in air dry oven and cut into circular disks, which were used as the working electrode. The counter electrode (lithium metal foil), separator (celgard 2502 membrane) and electrolyte (1 M LiPF<sub>6</sub> in ethylenecarbonate-diethyl carbon-dimethyl carbonate mixture (EC : DEC : DMC = 1 : 1 : 1)) were packaged with the working electrode in an argon-filled glove box (<1 ppm H<sub>2</sub>O, O<sub>2</sub>). The cycling stability and rate performance were tested using a NEWARE test system between 3.0 V and 10 mV. Cyclic voltammetry (CV) and impedance measurements were recorded using a CHI electrochemistry workstation (CHI604E).

## Results and discussion

The  $\gamma$ -Fe<sub>2</sub>O<sub>3</sub>@graphene material was synthesized in two steps, as shown in Scheme 1. PB and glucose were first stirred and then calcined under the condition of high temperature and reducing atmosphere and cooled down to room temperature. Then, the products of the first step were spontaneously oxidized in air and we obtained spherical  $\gamma$ -Fe<sub>2</sub>O<sub>3</sub>@graphene particles with different sizes (Fig. 1b). The small particle is a  $\gamma$ -Fe<sub>2</sub>O<sub>3</sub> core-shell monocrystalline structure with graphene layer, the larger one has a Fe layer between monocrystalline  $\gamma$ -Fe<sub>2</sub>O<sub>3</sub> and graphene layer (Fig. 1c and d), which is completely different from our previous study, which forms core-shell nano-polycrystalline hollow  $\gamma$ -Fe<sub>2</sub>O<sub>3</sub>@graphene at 650 °C *via* a simple Kirkendall process with oxidation at the room temperature.<sup>20</sup> To clarify the synthesis process and growth mechanism of monocrystalline  $\gamma$ -Fe<sub>2</sub>O<sub>3</sub>, we poured some water into the products of the first step before the samples were oxidized. Subsequently, we performed XRD and TEM immediately. From analyzing the XRD data and lattice fringes of the TEM images (Fig. 1e and f), we found that the intermediate product was monocrystalline Fe (JCPDS no. 89-7194), *i.e.*, there is a transformation process from monocrystalline Fe to monocrystalline  $\gamma$ -Fe<sub>2</sub>O<sub>3</sub>. This can help to understand why there are different sizes of particles of  $\gamma$ -Fe<sub>2</sub>O<sub>3</sub>, which should arise from



Scheme 1 The process of core-shell nano-monocrystalline  $\gamma$ -Fe<sub>2</sub>O<sub>3</sub>@graphene formation. The crystal structure of  $\gamma$ -Fe<sub>2</sub>O<sub>3</sub> in this graphic comes from part of Fig. S1,† which comprises FeO<sub>4</sub> tetrahedra and FeO<sub>6</sub> octahedra.

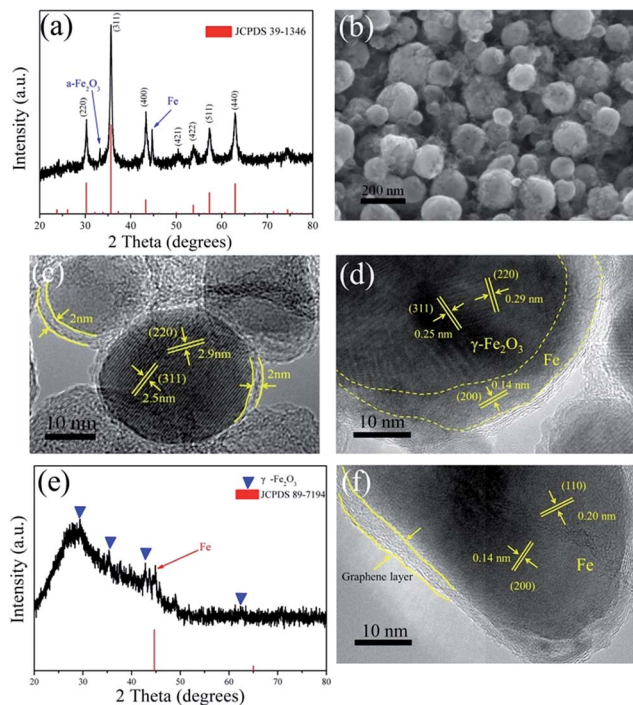


**Fig. 1** (a) The XRD data of monocrySTALLINE  $\gamma$ -Fe<sub>2</sub>O<sub>3</sub>@graphene; (b) the SEM image of monocrySTALLINE  $\gamma$ -Fe<sub>2</sub>O<sub>3</sub>@graphene with different particle sizes; (c and d) the TEM images of monocrySTALLINE  $\gamma$ -Fe<sub>2</sub>O<sub>3</sub>@graphene with different sizes; and (e and f) the XRD and TEM images of the intermediate products poured with water.

some Fe nanoparticles merging to form larger sizes so as to generate a size distribution observed for the final samples of  $\gamma$ -Fe<sub>2</sub>O<sub>3</sub> *via* an oxidation process as discussed below. When the nano-monocrySTALLINE Fe coated with graphene layers is exposed in air and in contact with oxygen, the nanoparticle Fe was oxidized and accompanied with open flames.

There may be two models to explain the process and mechanism from Fe nano-monocrySTALLINE to  $\gamma$ -Fe<sub>2</sub>O<sub>3</sub> nano-monocrySTALLINE. Model one is that the oxygen atoms, which come from splitting O<sub>2</sub> at the surface of nano-monocrySTALLINE Fe with Fe@graphene *via* interface catalysis,<sup>24</sup> are transmitted to the center of the monocrySTALLINE Fe (second step in Scheme 1).

When the oxygen atoms are gathered to reach a certain concentration around the Fe lattice, the oxygen atoms of the central part began to receive electrons from Fe and form a  $\gamma$ -Fe<sub>2</sub>O<sub>3</sub> monocrySTALLINE-“seed” domain. Then, as more oxygen atoms diffuse inside the Fe nano-monocrySTALLINE and grow along the existing  $\gamma$ -Fe<sub>2</sub>O<sub>3</sub> “seed” lattice, the nano-monocrySTALLINE  $\gamma$ -Fe<sub>2</sub>O<sub>3</sub> is grown from inside to outside, whereas the O atoms are diffused from outside to inside. Simultaneously, the well-coated graphene layer could effectively control the splitting of O<sub>2</sub>. By comparing the Fe and  $\gamma$ -Fe<sub>2</sub>O<sub>3</sub> crystal structures, the Fe crystal is body-centered cubic structure (middle figure of Scheme 1), when the O atoms are filled in the octahedral (FeO<sub>6</sub>) and tetrahedral (FeO<sub>4</sub>) spaces of the Fe crystal structure and as a result the  $\gamma$ -Fe<sub>2</sub>O<sub>3</sub> crystals would be formed and grown (right figure of Scheme 1 and Fig. S1†). Model two, which is different from Model one, is that the  $\gamma$ -Fe<sub>2</sub>O<sub>3</sub> monocrySTALLINE-“seed” (or

a domain) may be initially generated from one side of the surface at the interface of Fe@graphene, and then to grow up by diffusion of oxygen atoms along interface of the existing  $\gamma$ -Fe<sub>2</sub>O<sub>3</sub> “seed” domain and Fe crystal domain. Note that the experimental results can support both model one and two, by which the small Fe particles can completely be grown into the  $\gamma$ -Fe<sub>2</sub>O<sub>3</sub> nano-monocrySTALLINE. However, the large particles may not be grown completely as a full monocrySTALLINE with a Fe layer ( $\gamma$ -Fe<sub>2</sub>O<sub>3</sub>@Fe), as shown in Fig. 1d, because the activity for O<sub>2</sub> catalysis splitting and diffusion at Fe@graphene may decrease during the process. Now the question is what will be the key factor that leads to the difference in  $\gamma$ -Fe<sub>2</sub>O<sub>3</sub> nano-monocrySTALLINE growth observed in this study, when core-shell nanopolyCRYSTALLINE hollow  $\gamma$ -Fe<sub>2</sub>O<sub>3</sub>@graphene was formed in our previous study?<sup>20</sup> To compare the synthesis process of the present and previous study, the key difference is the calcination temperature of 950 °C and 650 °C in an argon atmosphere, respectively, in which the quality of the graphene layers and degree of compactness of the core-shell  $\gamma$ -Fe<sub>2</sub>O<sub>3</sub>@graphene formed at 950 °C (see Fig. 2a and b) was much better than that formed at 650 °C. The compact layers of graphene and sticking interface of Fe@graphene can make O<sub>2</sub> from the air diffuse slowly to the surface of the Fe nano-CRYSTALLINE, which is an advantage for controlling the growth of  $\gamma$ -Fe<sub>2</sub>O<sub>3</sub> as nano-monocrySTALLINE. In contrast, the loose layers of graphene and interface of Fe@graphene make O<sub>2</sub> diffuse rapidly to the Fe nano-CRYSTALLINE to form nano-polyCRYSTALLINE hollow  $\gamma$ -Fe<sub>2</sub>O<sub>3</sub>@graphene oxidation *via* a Kirkendall process.<sup>25</sup>

The crySTALLINE structure of the composite was checked by XRD in Fig. 1a, which showed three types of substances in the final mixture:  $\gamma$ -Fe<sub>2</sub>O<sub>3</sub>, Fe, and  $\alpha$ -Fe<sub>2</sub>O<sub>3</sub>. The main constituent was  $\gamma$ -Fe<sub>2</sub>O<sub>3</sub> and the seven diffraction peaks located at  $2\theta = 30.24^\circ, 35.63^\circ, 43.28^\circ, 50.00^\circ, 53.73^\circ, 57.27^\circ$  and  $62.92^\circ$  can be well assigned to  $\gamma$ -Fe<sub>2</sub>O<sub>3</sub> (JCPDS no. 39-1346, lattice constant  $a = b = c = 8.3515 \text{ \AA}$ ). No obvious characteristic peak of graphene may due to the overlap with the peaks of  $\gamma$ -Fe<sub>2</sub>O<sub>3</sub> at

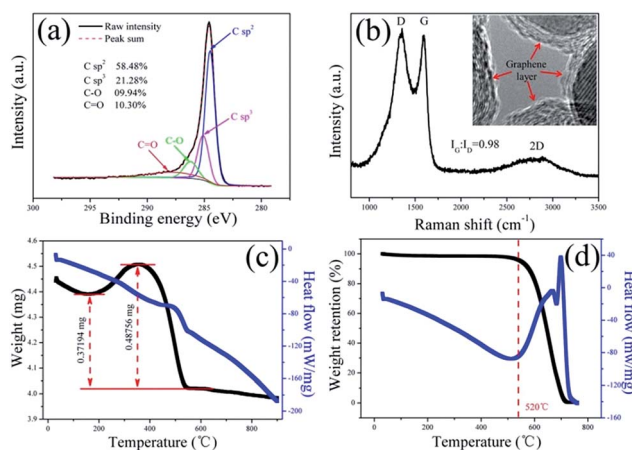


**Fig. 2** (a and b) X-ray photoelectron spectroscopy (XPS) spectra and Raman spectrum of monocrySTALLINE  $\gamma$ -Fe<sub>2</sub>O<sub>3</sub>@graphene; TGA and DTA curves of (c) monocrySTALLINE  $\gamma$ -Fe<sub>2</sub>O<sub>3</sub>@graphene and (d) burnt glucose (950 °C) in an air atmosphere.

26°. The peaks located at 711 eV and 724 eV correspond to Fe 2p<sub>3/2</sub> and Fe 2p<sub>1/2</sub>. There is a satellite peak between Fe 2p<sub>3/2</sub> and Fe 2p<sub>1/2</sub>, indicating that the composite contains Fe<sup>3+</sup> but not Fe<sup>2+</sup>. The peak located at 707 eV corresponds to Fe. The XPS results are in accordance with the XRD data (Fig. S2†). The SEM and TEM images of  $\gamma$ -Fe<sub>2</sub>O<sub>3</sub>@graphene are shown in Fig. 1b–d. The material has good dispersibility and the thickness of the graphene coating layer is about 2 nm. The coating layer has a high graphitization degree with a carbon sp<sup>2</sup> percentage of 58.48% (Fig. 2a). The peak positions of the four parts divided in the C1s XPS spectrum are 284.49 eV (carbon sp<sup>2</sup>), 285.1 eV (carbon sp<sup>3</sup>), 286.2 eV (C–O), and 287.8 eV (C=O). The Raman data shown in Fig. 2b also verified the graphitization degree of the composites, the ratio of I<sub>G</sub> and I<sub>D</sub> was 0.98. There also exists a 2D peak at about 2700 eV, which is the characteristic peak of graphene layers. The TEM image (inset in Fig. 2b) clearly shows the coating layer structure. To identify the carbon content, TGA was conducted. The material was heated in air conditions between 50 and 900 °C and we can observe that thermogravimetric curve has a increasing trend after 180 °C, which may be ascribed to the oxidation process of Fe (Fig. 2c). To confirm this, we also did a blank test and first calcined glucose at 950 °C under Ar and then subjected the product to TGA in air. It was found that there was no weight loss before 520 °C, as shown in Fig. 2d. We finally accurately determined the carbon weight of the composite to be below 16%.

Fig. 3a shows the charge–discharge curves of monocrystalline  $\gamma$ -Fe<sub>2</sub>O<sub>3</sub>@graphene for the first five cycles at 0.1C. One obvious voltage plateaus is located at 0.8 V during the initial discharge process. The discharge/charge specific capacities for the first cycle are 1513 and 1026 mA h g<sup>-1</sup> (contain both  $\gamma$ -Fe<sub>2</sub>O<sub>3</sub> and graphene), respectively, corresponding to a coulombic efficiency of 67.81% (Fig. S3†), which are higher than the theoretical capacity of Fe<sub>2</sub>O<sub>3</sub> (1007 mA h g<sup>-1</sup>). This irreversible capacity may arise from the decomposition of the electrolyte with the formation of a solid-electrolyte interphase (SEI). The cycle voltammograms of  $\gamma$ -Fe<sub>2</sub>O<sub>3</sub>@graphene are presented in Fig. 3b at 0.2 mV s<sup>-1</sup>. Two oxidation and reduction peaks were observed during the first cycle, in accordance with the first discharge–charge curves (Fig. 3a). The two oxidation peaks at 1.67 V and 1.79 V correspond to the two oxidation processes of Fe to Fe<sup>2+</sup> and Fe<sup>2+</sup> to Fe<sup>3+</sup>, respectively. The two reduction peaks located at 0.6 and 0.96 V can be attributed to the reversible conversion reaction of  $\gamma$ -Fe<sub>2</sub>O<sub>3</sub> with Li to form Li<sub>2</sub>O and the decomposition of the electrolyte to form SEI films. After the second cycle, only one cathodic peak at 0.82 V was observed, which hints the occurrence of some irreversible processes in the electrode material during the first cycle.

The cycle stability was checked at 1C and 5C for 600 cycles, as shown in Fig. 3c. We also offered the coulombic efficiency at a current density of 1C, as shown in Fig. S3† which are close to 98.92%. We find that the specific capacity increases during the first 80 cycles (the battery was treated at 0.1C for 5 cycles first). To figure out why the discharge specific capacity increased significantly during the first 80 cycles, we performed a TEM test with the electrode materials after 100 cycles, which involved crushing process (Fig. 3d and S4†). We also drew the charge/

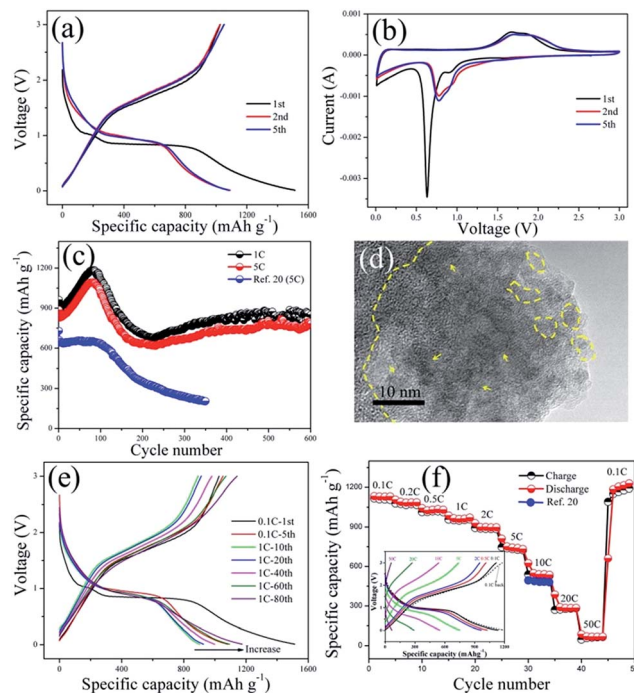


Fig. 3 The electrochemical performance of the prepared monocrystalline  $\gamma$ -Fe<sub>2</sub>O<sub>3</sub>@graphene. (a) Charge–discharge curves of monocrystalline  $\gamma$ -Fe<sub>2</sub>O<sub>3</sub>@graphene at 0.1C between 10 mV and 3.0 V for the first 5 cycles; (b) the cyclic voltammograms data of monocrystalline  $\gamma$ -Fe<sub>2</sub>O<sub>3</sub>@graphene at 0.2 mV s<sup>-1</sup>; (c) the cycle stability of monocrystalline  $\gamma$ -Fe<sub>2</sub>O<sub>3</sub>@graphene at 1C and 5C for 600 cycles and its comparison with our previous study at 5C (1C = 1000 mA g<sup>-1</sup>); (d) the TEM data of monocrystalline  $\gamma$ -Fe<sub>2</sub>O<sub>3</sub>@graphene after 100 cycles; (e) the charge–discharge curves of monocrystalline  $\gamma$ -Fe<sub>2</sub>O<sub>3</sub>@graphene at 1C for the first 80 cycles and (f) rate performances of monocrystalline  $\gamma$ -Fe<sub>2</sub>O<sub>3</sub>@graphene at 0.1, 0.2, 0.5, 1, 2, 5, 10, 20, and 50C, and its comparison with our previous study at 10C.

discharge curves of the first 80 cycles in Fig. 3e. The discharge curves above 0.8 V are ordinary, while the increasing part comes from the slope of the discharge curves between 0.8 V and 10 mV. When the monocrystalline  $\gamma$ -Fe<sub>2</sub>O<sub>3</sub>@graphene is pulverized during the charge–discharge process, the size of the active particles gets smaller to increase the surface area so as to enhance storage of Li-ions at the particle surfaces with protection of graphene-shell, which results in the capacity increase during the electrochemical process.<sup>8,39,40</sup>

We also made a comparison of the cycle stability with our previously reported study (Fig. 3c). It is clear that there is a big difference between the two materials at 5C. The specific capacity of monocrystalline  $\gamma$ -Fe<sub>2</sub>O<sub>3</sub>@graphene was 782.54 mA h g<sup>-1</sup> after 600 cycles at the rate of 5C, but the capacity of core–shell nano-hollow- $\gamma$ -Fe<sub>2</sub>O<sub>3</sub>@graphene decayed heavily after 100 cycles. The superior electrochemical performance can be attributed to the core–shell monocrystalline formed during the higher temperature calcination process, which can increase the high quality layers of graphene with the degree of carbonization to offer better buffering for the volume changes in the electrode material during the electrochemical process. Fig. 3f shows the rate capability at current densities of 0.1, 0.2, 0.5, 1, 2, 5, 10, 20

and 50C, with the corresponding capacities determined at 1132.04, 1088.02, 1030.79, 971.28, 897.75, 732.24, 535.86, 284.42, and 68.67 mA h g<sup>-1</sup>, respectively, which is higher than our previous materials at 10C (504 mA h g<sup>-1</sup>). At 0.1C, the discharge capacity can return to 1228 mA h g<sup>-1</sup>, demonstrating that the composite has a stable structure. The graphic inserted into Fig. 3f display the charge/discharge curves at different current densities. The impedance data in Fig. S5† also show that the material has good electrical conductivity when compared with our previous study. In a word, the compact graphene layer plays a key role in the electrochemical process.

## Conclusions

By increasing the calcination temperature, we obtained core-shell monocrystalline  $\gamma$ -Fe<sub>2</sub>O<sub>3</sub>@graphene composite with superior electrochemical performance. Moreover, we proposed the possible mechanism for the growth process from monocrystalline Fe to monocrystalline  $\gamma$ -Fe<sub>2</sub>O<sub>3</sub>. When compared to our previous study, the composite also shows much better electrochemical performance. The monocrystalline material can maintain 848.08 and 782.54 mA h g<sup>-1</sup> at 1C and 5C for 600 cycles, respectively. When evaluated at 10, 20 and 50C, the capacity still remained 535.86, 284.42 and 68.67 mA h g<sup>-1</sup>, respectively. Interestingly, the capacity increases during the initial cycles, which can be ascribed to an increase in Li-ion storage on the nanoparticle surfaces vs. an increase of surface area due to the pulverization of the monocrystalline  $\gamma$ -Fe<sub>2</sub>O<sub>3</sub> with protection of the strong graphene-shell. Taking into account this simple and general method, as well as the cheaper starting materials and superior electrochemical performance, this core-shell monocrystalline  $\gamma$ -Fe<sub>2</sub>O<sub>3</sub>@graphene composite may be a promising anode material for the next generation of lithium-ion batteries.

## Author contributions

Y. D. and F. P. contributed to the design of the experiments. J. H. and W. L. performed the experiments and analyzed the data. C. L. and H. T. carried out the sample tests such as XRD and SEM. T. L., H. G. and X. S. contributed to discuss the electrochemical results. J. Z. and Y. L. contributed to the preparation of this manuscript. J. H, Y. D., and F. P. wrote the manuscript. F. P. supervised the whole study.

## Acknowledgements

The study was financially supported by Guangdong Innovation Team Project (No. 2013N080) and Shenzhen Science and Technology Research Grant (peacock plan KYPT20141016105435850, JCYJ20150629144612861).

## References

- 1 M. Armand and J. M. Tarascon, *Nature*, 2008, **451**, 652–657.
- 2 B. Scrosati, *Nature*, 1995, **373**, 557–558.
- 3 Y. Nishi, *Chem. Rec.*, 2001, **1**, 406–413.

- 4 D. Deng, M. G. Kim, J. Y. Lee and J. Cho, *Energy Environ. Sci.*, 2009, **2**, 818–837.
- 5 J. Cabana, L. Monconduit, D. Larcher and M. Rosa Palacin, *Adv. Mater.*, 2010, **22**, E170–E192.
- 6 L. Zhang, H. B. Wu and X. W. Lou, *Adv. Energy Mater.*, 2014, **4**, 1032–1039.
- 7 J. Jiang, Y. Li, J. Liu, X. Huang, C. Yuan and X. W. Lou, *Adv. Mater.*, 2012, **24**, 5166–5180.
- 8 J. Luo, J. Liu, Z. Zeng, C. F. Ng, L. Ma, H. Zhang, J. Lin, Z. Shen and H. J. Fan, *Nano Lett.*, 2013, **13**, 6136–6143.
- 9 Y. Li, M. A. Trujillo, E. Fu, B. Patterson, L. Fei, Y. Xu, S. Deng, S. Smirnov and H. Luo, *J. Mater. Chem. A*, 2013, **1**, 12123–12127.
- 10 J. Lin, A.-R. O. Raji, K. Nan, Z. Peng, Z. Yan, E. L. G. Samuel, D. Natelson and J. M. Tour, *Adv. Funct. Mater.*, 2014, **24**, 2044–2048.
- 11 M. Rosa Palacin, *Chem. Soc. Rev.*, 2009, **38**, 2565–2575.
- 12 L. Xiao, M. Schroeder, S. Kluge, A. Balducci, U. Hagemann, C. Schulzad and H. Wiggers, *J. Mater. Chem. A*, 2015, **3**, 11566–11574.
- 13 S. Xu, C. M. Hessel, H. Ren, R. Yu, Q. Jin, M. Yang, H. Zhao and D. Wang, *Energy Environ. Sci.*, 2014, **7**, 632–637.
- 14 G. Wang, H. Wang, S. Cai, J. Bai, Z. Ren and J. Bai, *J. Power Sources*, 2013, **239**, 37–44.
- 15 B. Wang, H. Xin, X. Li, J. Cheng, G. Yang and F. Nie, *Sci. Rep.*, 2014, **4**, 1–7.
- 16 Z. Jian, B. Zhao, P. Liu, F. Li, M. Zheng, M. Chen, Y. Shi and H. Zhou, *Chem. Commun.*, 2014, **50**, 1215–1217.
- 17 Y. Li, C. Zhu, T. Lu, Z. Guo, D. Zhang, J. Ma and S. Zhu, *Carbon*, 2013, **52**, 565–573.
- 18 W.-J. Yu, P.-X. Hou, F. Li and C. Liu, *J. Mater. Chem.*, 2012, **22**, 13756–13763.
- 19 M. Y. Son, Y. J. Hong, J. K. Lee and Y. Chan Kang, *Nanoscale*, 2013, **5**, 11592–11597.
- 20 J. Hu, J. Zheng, L. Tian, Y. Duan, L. Lin, S. Cui, H. Peng, T. Liu, H. Guo, X. Wang and F. Pan, *Chem. Commun.*, 2015, **51**, 7855–7858.
- 21 E. Yoo, J. Kim, E. Hosono, H.-s. Zhou, T. Kudo and I. Honma, *Nano Lett.*, 2008, **8**, 2277–2282.
- 22 G. Wu, N. H. Mack, W. Gao, S. Ma, R. Zhong, J. Han, J. K. Baldwin and P. Zelenay, *ACS Nano*, 2012, **6**, 9764–9776.
- 23 L. Liu, Y.-P. Zhu, M. Su and Z.-Y. Yuan, *ChemCatChem*, 2015, **7**, 2765–2787.
- 24 X. Wang, Q. Li, H. Pan, Y. Lin, Y. Ke, H. Sheng, M. T. Swihart and G. Wu, *Nanoscale*, 2015, **7**, 20290–20298.
- 25 Y. Yin, R. M. Rioux, C. K. Erdonmez, S. Hughes, G. A. Somorjai and A. P. Alivisatos, *Science*, 2004, **304**, 711–714.
- 26 G.-W. Zhou, J. Wang, P. Gao, X. Yang, Y.-S. He, X.-Z. Liao, J. Yang and Z.-F. Ma, *Ind. Eng. Chem. Res.*, 2013, **52**, 1197–1204.
- 27 J. Qu, Y. X. Yin, Y. Q. Wang, Y. Yan, Y. G. Guo and W. G. Song, *ACS Appl. Mater. Interfaces*, 2013, **5**, 3932–3936.
- 28 G. Bhargava, I. Gouzman, C. M. Chun, T. A. Ramanarayanan and S. L. Bernasek, *Appl. Surf. Sci.*, 2007, **253**, 4322–4329.
- 29 Z. Y. Sun, H. Q. Yuan, Z. M. Liu, B. X. Han and X. R. Zhang, *Adv. Mater.*, 2005, **17**, 2993–2997.

- 30 Y. Wang, H. Sun, X. Duan, H. M. Ang, M. O. Tadé and S. Wang, *Appl. Catal., B*, 2015, **172–173**, 73–81.
- 31 V. Chandra, J. Park, Y. Chun, J. W. Lee, I. C. Hwang and K. S. Kim, *ACS Nano*, 2010, **4**, 3979–3986.
- 32 P. Merel, M. Tabbal, M. Chaker, S. Moisa and J. Margot, *Appl. Surf. Sci.*, 1998, 105–110.
- 33 Y.-P. Zhu, T.-Z. Ren, Y.-P. Liu and Z.-Y. Yuan, *RSC Adv.*, 2014, **4**, 31754–31758.
- 34 M. A. Pimenta, G. Dresselhaus, M. S. Dresselhaus, L. G. Cancado, A. Jorio and R. Saito, *Phys. Chem. Chem. Phys.*, 2007, **9**, 1276–1291.
- 35 G.-W. Zhou, J. Wang, P. Gao, X. Yang, Y.-S. He, X.-Z. Liao, J. Yang and Z.-F. Ma, *Ind. Eng. Chem. Res.*, 2013, **52**, 1197–1204.
- 36 Z. Wang, D. Luan, S. Madhavi, Y. Hu and X. W. Lou, *Energy Environ. Sci.*, 2012, **5**, 5252–5256.
- 37 H. Liu, G. Wang, J. Park, J. Wang, H. Liu and C. Zhang, *Electrochim. Acta*, 2009, **54**, 1733–1736.
- 38 G. W. Zhou, J. Wang, P. Gao, X. Yang, Y. S. He, X. Z. Liao, J. Yang and Z. F. Ma, *Ind. Eng. Chem. Res.*, 2013, **52**, 1197–1204.
- 39 M. F. Hassan, Z. Guo, Z. Chen and H. Liu, *Mater. Res. Bull.*, 2011, **46**, 858–864.
- 40 X. Huang, J. Chen, Z. Lu, H. Yu, Q. Yan and H. H. Hng, *Sci. Rep.*, 2013, **3**, 2317–2326.